



Contents lists available at ScienceDirect

# Computer Physics Communications

journal homepage: [www.elsevier.com/locate/cpc](http://www.elsevier.com/locate/cpc)

## MULTI-IFE—A one-dimensional computer code for Inertial Fusion Energy (IFE) target simulations<sup>☆</sup>

R. Ramis<sup>a,\*</sup>, J. Meyer-ter-Vehn<sup>b</sup><sup>a</sup> E.T.S.I. Aeronáutica y del Espacio, Universidad Politécnica de Madrid, Spain<sup>b</sup> Max-Planck-Institut für Quantenoptik, Garching, Germany

### ARTICLE INFO

#### Article history:

Received 31 July 2015

Received in revised form

21 January 2016

Accepted 8 February 2016

Available online 24 February 2016

#### Keywords:

Inertial confinement fusion

Radiation transport

Computational methods in gas dynamics

Thermonuclear ignition

### ABSTRACT

The code MULTI-IFE is a numerical tool devoted to the study of Inertial Fusion Energy (IFE) microcapsules. It includes the relevant physics for the implosion and thermonuclear ignition and burning: hydrodynamics of two component plasmas (ions and electrons), three-dimensional laser light ray-tracing, thermal diffusion, multigroup radiation transport, deuterium–tritium burning, and alpha particle diffusion. The corresponding differential equations are discretized in spherical one-dimensional Lagrangian coordinates. Two typical application examples, a high gain laser driven capsule and a low gain radiation driven marginally igniting capsule are discussed. In addition to phenomena relevant for IFE, the code includes also components (planar and cylindrical geometries, transport coefficients at low temperature, explicit treatment of Maxwell's equations) that extend its range of applicability to laser–matter interaction at moderate intensities ( $< 10^{16}$  W cm<sup>-2</sup>). The source code design has been kept simple and structured with the aim to encourage user's modifications for specialized purposes.

#### Program summary

*Program title:* MULTI-IFE

*Catalogue identifier:* AEZR\_v1\_0

*Program summary URL:* [http://cpc.cs.qub.ac.uk/summaries/AEZR\\_v1\\_0.html](http://cpc.cs.qub.ac.uk/summaries/AEZR_v1_0.html)

*Program obtainable from:* CPC Program Library, Queen's University, Belfast, N. Ireland

*Licensing provisions:* Standard CPC licence, <http://cpc.cs.qub.ac.uk/licence/licence.html>

*No. of lines in distributed program, including test data, etc.:* 267428

*No. of bytes in distributed program, including test data, etc.:* 3798542

*Distribution format:* tar.gz

*Programming language:* Fortran 95.

*Computer:* Any.

*Operating system:* Any.

*RAM:* 1.8 MB

*Classification:* 19.7.

*Nature of problem:* The implosion and ignition of inertial energy fusion capsules driven either directly by laser beams or indirectly by thermal radiation.

*Solution method:* The one-dimensional equations of hydrodynamic motion, laser propagation, energy transport by thermal conduction and radiative transfer, deuterium–tritium thermonuclear burning, and  $\alpha$ -particle diffusion are discretized on a Lagrangian grid, and advanced in time by a fractional step scheme. An implicit conservative method is used to treat hydrodynamics. Thermal and electrical conductivities as well as coefficients for laser absorption and electron–ion energy exchange are obtained from a two

<sup>☆</sup> This paper and its associated computer program are available via the Computer Physics Communication homepage on ScienceDirect (<http://www.sciencedirect.com/science/journal/00104655>).

\* Correspondence to: E.T.S.I. Aeronáutica y del Espacio, P. Cardenal Cisneros 3, 28040 Madrid, Spain. Tel.: +34 913363938.

E-mail address: [rafael.ramis@upm.es](mailto:rafael.ramis@upm.es) (R. Ramis).

temperature (for electrons and ions) model. Laser propagation is treated by 3D tracing of the laser rays in the geometrical optics approximation. Radiation transfer is solved by using the forward–reverse method for a discrete number of frequency groups. Matter properties are interpolated from tables (equations-of-state, ionization, and opacities) generated by external codes.

*Restrictions:* The code has been designed for typical conditions prevailing in inertial confinement fusion (ps–ns time scale, matter states close to local thermodynamic equilibrium, and negligible radiation pressure). A wider range of situations can be treated, as long as the above conditions are fulfilled. This includes, in particular, laser plasma experiments at moderate intensities ( $\leq 10^{16}$  W cm $^{-2}$ ).

*Unusual features:* An optional graphical post-processing package is included in the distribution. This option requires a Linux/Unix operating system with the essential developing tools (C compiler; X11 libraries and include files; and the xterm command). Most of the figures in this paper have been created using this software.

*Additional comments:* The source code design has been kept simple and structured, with the aim to encourage user's modifications for specialized purposes. A technical manual is included in the package.

*Running time:* 13–18 s for the examples discussed in the paper.

© 2016 Elsevier B.V. All rights reserved.

## 1. Introduction

Inertial Fusion Energy (IFE) [1–4] represents one of the two main approaches to the civilian exploitation of nuclear fusion energy. IFE production is based on the implosion and ignition of spherical microcapsules containing few milligrams of deuterium–tritium mixture. Implosion can be driven by either direct irradiation of the capsules by laser beams (direct drive) or by exposing the capsules to a high temperature thermal radiation (indirect drive). Because of the huge size and costs of experimental facilities and the complexity and difficulty of diagnostics, a substantial part of the research in this field relies on numerical simulations. The code MULTI-IFE described in the present paper implements a one-dimensional spherical model that includes the basic physical phenomena required to simulate and study IFE targets: two-temperature hydrodynamics, laser light absorption, heat conduction, multi-group radiation transport, thermonuclear burn, and  $\alpha$ -particle transport. The study of the important multi-dimensional effects such as hydrodynamic instabilities and mixing processes remain outside the scope of this code. Even though these multi-dimensional effects have turned out to be a key issue in the recent NIC experiments [5], codes like MULTI-IFE are useful for quick orientation when changing designs and drive parameters. One of the two designs discussed in this paper is also used in the book [3] as a representative example for IFE targets. The code MULTI-IFE allows for detailed studies of such designs.

A substantial part of the physics included in the code was already present in the widely used codes MULTI [6] and MULTI-fs [7,8], devoted to the analysis of experiments of laser irradiated targets. In order to keep these capabilities, the treatment of laser light by explicit solution of Maxwell's equations (in planar targets) and the computation of low temperature transport coefficients, though not so important in IFE applications, are still present in MULTI-IFE and can be switched on to use the code in a wider range of applications. Some of these applications require specific settings that are not available in the standard version of the code (additional energy deposition mechanisms, customized output, special boundary conditions, etc.). To facilitate the user to modify the code to fit to his needs, the structure of the Fortran source has been kept simple (one file), compact (4356 lines), and clear (data organized in hierarchical structures). A technical manual, supplied with the source code, explains in detail data structures, flowchart, file formats, input parameters, installation procedure, and several examples. In this paper we describe the physical model

and the numerical methods used by the code. For consistency and completeness, the components relating to the MULTI-fs code, are also briefly described, but we refer the reader to [8] for details. In Sections 2–5, the equations describing hydrodynamics, thermal flux, electron–ion relaxation, radiation transport, and their discretization are discussed. The specific IFE features, namely, a 3D laser ray tracing package and a thermonuclear burn package, are discussed in detail in Sections 6 and 7, respectively. The structure of the code is briefly discussed in Section 8. In Sections 9 and 10, two representative IFE examples are presented, a direct drive target and an indirect drive target, respectively.

## 2. IFE radiation hydrodynamics

The physics of IFE targets involves several concurrent processes. A spherical micro-capsule containing thermonuclear fuel is irradiated by either laser light (direct drive) or by soft X-rays (indirect drive). In indirect drive, the capsule is placed inside a small cavity. X-rays are generated by heating such cavity by laser beams [2], heavy ion beams [9], or high current discharges [10]. In both direct and indirect drive the energy absorbed in the outer plasma corona of evaporated material is transported inwards, leading to further material ablation. This process induces the implosion of the inner part of the capsule leading to extreme conditions in the imploded center. At sufficient temperature, thermonuclear reactions set in. Reaction products, in particular  $\alpha$ -particles, are reabsorbed, heating the plasma and boosting the burning process. All transport mechanisms (thermal X-rays, fusion products, and electron and ion heat diffusion) play an important role and have to be consistently modeled. To integrate all this phenomena in a computer code, a modular design is required.

The state of the matter is modeled here as a two component plasma fluid described by continuous variables depending on position and time. IFE plasmas are quasi-neutral; the number densities of electrons  $n^e$  and ions  $n^i$  satisfy  $zn^i \simeq n^e$ , where  $z$  is the average ionization. Both densities can be expressed in terms of a unique mass density  $\rho \simeq am_p n^i$ , where  $a$  is the average atomic number and  $m_p$  the proton mass. In finite one-dimensional plasmas, there is no net current density,  $zn^i v^i - n^e v^e \simeq 0$ ; as a consequence, both species have the same fluid velocity  $v \simeq v^e \simeq v^i$ . On the other hand, due to the big difference between electron and ion masses, the two species thermalize separately with different temperatures,  $T^e$  and  $T^i$ , respectively. Thermodynamic matter properties can be obtained from the QEOS

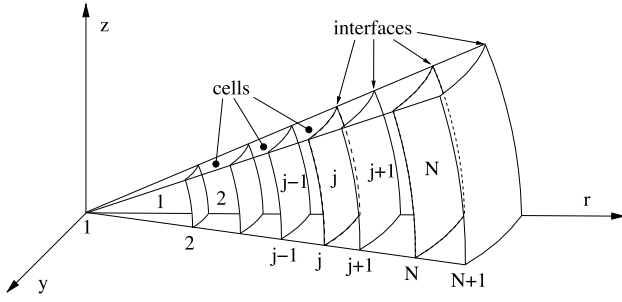


**Fig. 1.** Staggered grid (spherical geometry). Scalar quantities are defined at cells, and vectorial ones defined at interfaces.

model [11,12], where the thermodynamic free energy is modeled as the sum of electron and ion contributions plus a binding correction. Specific internal energies ( $e^e$  and  $e^i$ ) and pressures ( $P^e$  and  $P^i$ ) for electron and ion species are derived as functions of mass density, and electron and ion temperatures. The code uses a Lagrangian description of the fluid; instead of the space coordinate  $r$ , the mass coordinate

$$\mu(r, t) = \int_0^r \rho(r, t) 4\pi r^2 dr \quad (1)$$

is taken as an independent variable. For a particle moving with the fluid, the value of  $\mu$  is constant. Also, in absence of diffusion and reactions, the fluid composition is constant at a given value of  $\mu$ . This allows us to use, as state variables, the specific internal energies of electrons  $e^e(\mu, t)$  and ions  $e^i(\mu, t)$ , together with fluid position  $r(\mu, t)$  and velocity  $v(\mu, t)$ . Mass density, temperatures, pressures, ionization, and other quantities can be expressed in terms of these variables. When thermonuclear reactions set in, two additional variables are included in the set of state variables: the molar fraction of deuterium,  $f(\mu, t)$ , and the specific energy of non-thermalized  $\alpha$ -particles,  $e^\alpha(\mu, t)$ .

The problem will be discretized in two steps: semi-discretizations in space and in time. First, the above continuous functions are discretized on the staggered grid schematized in Fig. 1. The control particles (with constant value of  $\mu$ ) that define the Lagrangian grid are represented as spherical surfaces (called interfaces) and numbered from 1 to  $N + 1$ . The regions between interfaces (called cells) are numbered from 1 to  $N$ . Cell  $j$  is located between interfaces  $j$  and  $j + 1$ , while interface  $j$  separates cell  $j - 1$  from cell  $j$ . In general, vectorial quantities (like position  $r_j$  and velocity  $v_j$ ) are defined at interfaces, while scalar quantities (like specific energies  $e_j^e$ ,  $e_j^i$ , and  $e_j^\alpha$ , and the molar fraction of deuterium  $f_j$ ) are defined at cell centers. The state vector  $\mathbf{X}(t)$  of the semi-discretized problem comprises a finite number of continuous functions of time whose evolution is governed by a set of ordinary differential equations

$$\frac{d\mathbf{X}}{dt} = \mathbf{F}(\mathbf{X}, t). \quad (2)$$

Direct integration of this system by a standard explicit method (e.g. a fourth order Runge–Kutta scheme) would require, in typical situations, a prohibitively small time step. This is due to the parabolic nature of the equations for heat (or radiation) transport. On the other hand, an implicit method would be inefficient and cumbersome to implement because radiative transport couples all cells with each other, leading to a fully filled Jacobian matrix  $\partial\mathbf{F}/\partial\mathbf{X}$ . Here, a fractional step method (also called operator-splitting method) has been adopted. The right-hand side of Eq. (2) is decomposed as a sum of  $N_p$  subprocesses

$$\frac{d\mathbf{X}}{dt} = \sum_{k=1}^{N_p} \mathbf{F}_k(\mathbf{X}, t). \quad (3)$$

The values of the state vector at discretized times,  $\mathbf{X}^n \equiv \mathbf{X}(t^n)$ , are obtained assuming that the terms on the right-hand side of this equations act successively in the course of an integration step. Let  $\mathbf{Y}_i$  be the intermediate value of the state vector after the  $i$ th subprocess. One sets  $\mathbf{Y}_1(t^n) = \mathbf{X}^n$  and integrates one by one the  $N_p$  differential equations

$$\frac{d\mathbf{Y}_k}{dt} = \mathbf{F}_k(\mathbf{Y}_k, t), \quad (4)$$

from  $t^n$  to  $t^{n+1}$ , using  $\mathbf{Y}_k(t^n) = \mathbf{Y}_{k-1}(t^{n+1})$  as initial condition, to finally obtain  $\mathbf{X}^{n+1} = \mathbf{Y}_{N_p}(t^{n+1})$ . It can be shown that the truncation error of this procedure is proportional to  $(t^{n+1} - t^n)^2$ , so that the method is only first order accurate in time. The great advantage is that Eq. (4) involves only part of the problem, and can be solved in a compact and efficient way (e.g., in the implicit solver used for radiation transport, the Jacobian matrix reduces to a tridiagonal matrix when each group is solved individually). The simplicity and flexibility of the method compensates by far its rather poor temporal accuracy. The distinct algorithms applied to each subprocess will be explained in the next five sections.

### 3. Hydrodynamics

During this subprocess, the values of  $r_j$ ,  $v_j$ ,  $e_j^e$ ,  $e_j^i$ , and  $e_j^\alpha$  are advanced in time, ignoring any external source of energy. The space discretized momentum equation is

$$\lambda m_{j-1} \frac{dv_{j-1}}{dt} + \left( \frac{1}{2} - \lambda \right) (m_{j-1} + m_j) \frac{dv_j}{dt} + \lambda m_j \frac{dv_{j+1}}{dt} = A_j (P_{j-1} - P_j), \quad (5)$$

where  $m_j$  denotes the mass of the cell  $j$ .  $A_j$  are the areas associated to the interfaces (1,  $2\pi r_j$ , and  $4\pi r_j^2$ , for planar, cylindrical, and spherical geometry, respectively),  $P_j \equiv P_j^e + P_j^i + P_j^\alpha$  are the total cell pressures, and  $\lambda$  is a numerical parameter. For the first and last interfaces,  $m_0 = m_{N+1} = 0$  is taken. At these places one can assume either a freely expanding fluid (external zero pressure:  $P_0 = 0$  or  $P_{N+1} = 0$ ), or a rigid boundary (using  $v_1 = 0$  or  $v_{N+1} = 0$  instead Eq. (5)). The equations for the specific energies are

$$m_j \frac{de_j^k}{dt} = -P_j^k (A_{j+1} v_{j+1} - A_j v_j), \quad (6)$$

where the superscript  $k$  indicates the species ( $k = e, i, \text{ or } \alpha$ ). For electrons and ions,  $P_j^e$  and  $P_j^i$  are interpolated in tables as functions of mass density  $\rho_j$  and specific internal energies  $e_j^e$  and  $e_j^i$ . For  $\alpha$ -particles, an ideal gas equation of state is assumed:  $P_j^\alpha = \frac{2}{3} e_j^\alpha \rho_j$ . In addition, an artificial viscosity term  $P_j^v$  is needed to treat numerically the dynamics of shock waves. Since in a plasma, viscosity effects are mainly due to the ions, this term is added to  $P_j^i$ . Using

$$P_j^v = A^2 \rho_j (\min(0, v_{j+1} - v_j))^2, \quad (7)$$

where  $A$  is a constant of order unity, shock waves appear as strong gradient layers that spread over a few ( $\simeq A$ ) cells [13]. Pressures are directly available at the beginning of the time step, when internal energies and densities are accessible as part of the state vector. At other times, pressures are linearly extrapolated

$$\bar{P}_j^k(t) = P_j^k(t^n) + \left( \frac{\partial P_j^k}{\partial \rho_j} \right)_s (\rho_j(t) - \rho_j(t^n)). \quad (8)$$

The partial derivative in this equation, the squared adiabatic sound velocity, is evaluated at the beginning of the integration step. The effective pressure is taken as a combination of extrapolated

pressures at the beginning ( $t^n$ ), at intermediate time ( $t^* = t^n + \Delta t/2$ ), and at the end ( $t^{n+1} = t^n + \Delta t$ ) of the integration interval

$$P_j^{k,*} = 2\alpha \bar{P}_j^k(t^{n+1}) + (1 - 2\alpha - 2\beta) \bar{P}_j^k(t^*) + 2\beta \bar{P}_j^k(t^n), \quad (9)$$

where  $\alpha$  and  $\beta$  are numerical coefficients. The effective pressure is assumed to act impulsively. At  $t^*$ , the velocities of interfaces change instantaneously from  $v_j^n$  to  $v_j^{n+1}$ . The position of interfaces is thus given by

$$r_j^* = r_j^n + v_j^n \frac{\Delta t}{2}, \quad (10)$$

$$r_j^{n+1} = r_j^* + v_j^{n+1} \frac{\Delta t}{2}. \quad (11)$$

The values of  $A_j$  in Eqs. (5) and (6) are computed from  $r_j^*$ . The velocities to be used in Eqs. (6) turn out to be  $\frac{1}{2}(v_j^n + v_j^{n+1})$ . For the viscous stress in Eq. (7), one can use a combination of velocities:  $(1-s)v_j^n + sv_j^{n+1}$ , where  $s$  is a numerical factor. The hydrodynamic algorithm is implicit because effective pressures  $P_j^{k,*}$  depend on the density at  $t^{n+1}$ , that in turn depends, through  $r_j^{n+1}$  and  $v_j^{n+1}$ , on the effective pressures. The coupled set of Eqs. (5)–(11) reduces to a tridiagonal system that can be easily solved. The accuracy and stability of the method will be analyzed in a separate numerical study. It can be shown that energy is preserved. Here, to guarantee a robust behavior in a wide range of situations, the values of the numerical parameters have been hard-coded to  $\alpha = 1$ ,  $\beta = \lambda = 0$ ,  $A^2 = 2$  and  $s = 1$ .

#### 4. Heat transport

The heat transport algorithm advances the specific energies of electrons and ions by solving the diffusive transfer and energy exchange equations. Hydrodynamic motion, nuclear reactions, and other transport phenomena (by radiation or  $\alpha$ -particles) are ignored in this subprocess. The energy equations are

$$m_j \frac{de_j^e}{dt} = A_j S_j^e - A_{j+1} S_{j+1}^e - m_j K_j^{ei} (T_j^e - T_j^i) + Q_j^e, \quad (12)$$

$$m_j \frac{de_j^i}{dt} = A_j S_j^i - A_{j+1} S_{j+1}^i + m_j K_j^{ei} (T_j^e - T_j^i) + Q_j^i, \quad (13)$$

where  $S_j^e$  and  $S_j^i$  are the thermal fluxes carried by electrons and ions, respectively. Both are assumed to be zero at the boundaries ( $S_1^k = S_{N+1}^k = 0$ ). The term with coefficient  $K_j^{ei}$  is the power exchange between electrons and ions.  $Q_j^e$  and  $Q_j^i$  are the power depositions due to laser absorption and  $\alpha$ -particle heating (see Section 8.2). In a plasma with gentle temperature gradients

$$S_j^e = -(K^e \nabla T^e)_j = -K_j^e \frac{T_j^e - T_{j-1}^e}{\frac{1}{2}(r_{j+1} - r_{j-1})}, \quad (14)$$

$$S_j^i = -(K^i \nabla T^i)_j = -K_j^i \frac{T_j^i - T_{j-1}^i}{\frac{1}{2}(r_{j+1} - r_{j-1})}. \quad (15)$$

The thermal conductivity for electrons can be expressed [14] as

$$K^e = \alpha(z) \frac{n^e k^2 T^e}{m_e v^e}, \quad (16)$$

where  $n^e$  is the electron number density,  $z$  is the average ion charge,  $k$  is Boltzmann's constant,  $m_e$  is the electron mass, and  $v^e$  is the electron collision frequency. The numerical coefficient  $\alpha(z)$  can be approximated by the expression  $\alpha(z) \simeq 3.23(z + 0.24)/(1 + 0.24z)$ . Under some irradiation conditions, extreme temperature gradients may occur so that Eq. (14) does not apply any more. In

order to deal roughly with such situations, the heat flux is limited according to [3, 15, 16]

$$|S^e| \leq S_{max}^e \equiv f n^e k T^e \sqrt{\frac{k T^e}{m_e}}, \quad (17)$$

where the flux limit  $S_{max}^e$  is set to the physical maximum, reduced by an empirical factor  $f$  (see [3], Chap. 7.2). This limitation is enforced in the code by using the modified conductivity

$$\hat{K}^e = \frac{K^e S_{max}^e}{S_{max}^e + K^e |\nabla T^e|}, \quad (18)$$

instead of  $K^e$  in Eq. (14). This quantity is evaluated using the interface centered values  $K_j^{e,int}$  and  $S_{max,j}^{e,int}$  interpolated from cell centered quantities

$$K_j^{e,int} = \frac{1}{4} \left( \frac{K_{j-1}^{e,cell}}{(T_{j-1}^e)^{3/2}} + \frac{K_j^{e,cell}}{(T_j^e)^{3/2}} \right) ((T_{j-1}^e)^{3/2} + (T_j^e)^{3/2}), \quad (19)$$

$$S_{max,j}^{e,int} = \frac{fk^{3/2}}{8m_p m_e^{1/2}} \left( \frac{z_{j-1}}{a_{j-1}} + \frac{z_j}{a_j} \right) \times ((T_{j-1}^e)^{3/2} + (T_j^e)^{3/2}) (\rho_{j-1} + \rho_j), \quad (20)$$

where  $a_j$  is the average mass number at cell centers. The coefficient for energy exchange between electrons and ions [14] (Eq. 2.17) is evaluated at cell centers

$$K_j^{ei} = \frac{3m_e z_j v_j^e k}{a_j^2 m_p^2}. \quad (21)$$

The ion thermal conductivity in a high temperature plasma, is related to the electron heat conductivity by [17]

$$\frac{K^i}{K^e} = \frac{\beta(z)}{z^3} \sqrt{\frac{m_e}{am_p}} \left( \frac{T^i}{T^e} \right)^{5/2}, \quad (22)$$

where  $\beta(z)$  is a numerical factor that is set equal to one. Notice that, due to the fact that  $m_p \gg m_e$ , the ion thermal flux is negligible for  $T^e \simeq T^i$ . Nevertheless, in IFE implosions, when the first shock arrives to the center, due to viscous dissipation, a strong ion temperature peak occurs. In fact, in pure hydrodynamics, temperature becomes singular. The addition of ion heat diffusion smoothes the ion temperature profiles and avoids the appearance of such singularities. In all other situations, ion thermal flux can be neglected. The ion conductivity at interfaces is interpolated from cell centered values

$$K_j^{i,int} = \frac{1}{2} (K_{j-1}^{i,cell} + K_j^{i,cell}) \quad (23)$$

and no flux limitation is considered for ion thermal flux. The time derivatives of energy in Eqs. (12) and (13) are linearized as

$$\frac{de_j^k}{dt} \simeq \frac{\Delta e_j^k}{\Delta t} \simeq \left( \frac{\partial e_j^k}{\partial T_j^k} \right)_\rho \frac{T_j^{k,n+1} - T_j^{k,n}}{\Delta t} = c_{v,j}^k \frac{T_j^{k,n+1} - T_j^{k,n}}{\Delta t}. \quad (24)$$

The specific heat capacities  $c_{v,j}^e$  and  $c_{v,j}^i$ , and the coefficients  $\hat{K}_j^e$ ,  $K_j^i$ , and  $K_j^{ei}$  are evaluated from the values of temperature at the beginning of the time step. Eqs. (12) and (13) become a linear implicit system in  $T_j^{e,n+1}$  and  $T_j^{i,n+1}$ , that will be split into two subprocesses. In the first,  $S^i$  terms are ignored. In the second, only these terms are considered. Both subprocesses reduce to tridiagonal systems. The electron collision frequency in Eqs. (16) and (21) is also needed to compute laser attenuation [8]. For high temperature ideal plasma, the collision frequency is given by Eq. 10.133 in [3]. This is the situation found in IFE plasmas. For

low temperature plasmas, two different models are included in the code: one based on electron scattering by electron–phonon interaction [7], and the other based on the Drude–Sommerfeld model [18,19].

## 5. Radiation transport

Radiation transport plays an important role in IFE targets. For indirectly driven targets, it transfers the energy from beam heated regions to the imploding fuel capsule. Radiation cooling is crucial when ignition conditions are reached, imposing strong constraints to target design (e.g., fixing a temperature threshold  $\gtrsim 5$  keV for ignition). The quasi-static radiation transport model derived in [8] has been implemented. Only the specific energy of electrons  $e_j^e$  is modified by the radiation subprocess. The photon spectra is discretized in  $N_G$  groups. Group  $k$  is defined as the set of photons whose frequency  $\nu$  lies inside the interval from  $\nu_k$  to  $\nu_{k+1}$ . Energy density and flux are

$$U^k(r, t) = \frac{1}{c} \int_{\nu_k}^{\nu_{k+1}} \int_0^\pi I(r, \theta, \nu, t) 2\pi \sin \theta d\theta d\nu, \quad (25)$$

$$S^k(r, t) = \int_{\nu_k}^{\nu_{k+1}} \int_0^\pi \cos \theta I(r, \theta, \nu, t) 2\pi \sin \theta d\theta d\nu, \quad (26)$$

where  $c$  is the light velocity,  $\theta$  is the angle between the direction of photon propagation and the radial direction, and  $I(r, \theta, \nu, t)$  is the spectral intensity, i.e. the energy flux per unit of solid angle and frequency.  $U^k$  and  $S^k$  are discretized at cell centers and at interfaces, respectively. The subprocess for group  $k$  is specified by

$$m_j \frac{de_j^e}{dt} = A_j S_j^k - A_{j+1} S_{j+1}^k + Q_j^k, \quad (27)$$

$$A_j S_j^k - A_{j+1} S_{j+1}^k = -c \chi_j^{P,k} (\epsilon_j^k U^{P,k}(T_j^e) - U_j^k) V_j, \quad (28)$$

$$\frac{c}{2} \frac{U_j^k - U_{j-1}^k}{r_{j+1} - r_{j-1}} = -\hat{\chi}_j^k S_j^k, \quad (29)$$

where  $V_j$  is the cell volume and  $Q_j^k$  is the specific laser power deposition coupled to the group (see Section 8.2). The Planckian energy density is

$$U^{P,k}(T) = \frac{4\pi}{c} \int_{\nu_k}^{\nu_{k+1}} I^P(\nu, T) d\nu, \quad (30)$$

where

$$I^P(\nu, T) = \frac{2h\nu^3}{c^2(e^{h\nu/kT} - 1)}. \quad (31)$$

The apparent opacity (combining optical and geometrical effects) is

$$\hat{\chi}_j^k = \frac{2}{\frac{1}{\chi_j^{R,k}} + \frac{1}{\chi_{j-1}^{R,k}}} + \frac{\left(\frac{2r_j}{r_{j+1}+r_{j-1}}\right)^d - \left(\frac{2r_j}{r_j+r_{j+1}}\right)^d}{r_{j+1} - r_{j-1}}, \quad (32)$$

where  $d$  is 0, 1, and 2, for planar, cylindrical, and spherical geometries.  $\chi^{R,k}$ ,  $\chi^{P,k}$ , and  $\epsilon^k$  are the so called Rosseland average opacity, Planck average opacity, and normalized emissivity, that are defined as

$$\chi^{R,k} = \int_{\nu_k}^{\nu_{k+1}} \frac{\partial I^P}{\partial T} d\nu \bigg/ \int_{\nu_k}^{\nu_{k+1}} \frac{1}{\chi} \frac{\partial I^P}{\partial T} d\nu, \quad (33)$$

$$\chi^{P,k} = \int_{\nu_k}^{\nu_{k+1}} \chi I^P d\nu \bigg/ \int_{\nu_k}^{\nu_{k+1}} I^P d\nu, \quad (34)$$

$$\epsilon^k = \int_{\nu_k}^{\nu_{k+1}} \eta d\nu \bigg/ \int_{\nu_k}^{\nu_{k+1}} \chi I^P d\nu, \quad (35)$$

where  $\chi(\nu, \rho, T)$  and  $\eta(\nu, \rho, T)$  are the spectrally resolved opacity and emissivity. Notice that  $\epsilon^k$  reduces to unity in case of thermodynamic equilibrium because, by the Kirchhoff's law,  $\eta = \chi I^P$ . The values of  $\chi$  and  $\eta$  have to be obtained from atomic physics models. In the examples of Sections 9 and 10, these quantities have been computed by the code SNOB [20,21] as functions of frequency, matter density, and matter temperature, by assuming either thermodynamic equilibrium (for high density) or coronal equilibrium (for low density). Because most of the radiative phenomena are due to electrons, electron temperature is used to evaluate opacity and emissivity. Eq. (29) is not defined for  $j = 1$  and  $j = N + 1$ , so that boundary conditions should be used to determine the radiative flux there. According to the forward–reverse approximation [22,8], the value of  $S^k$  at the external boundary can be evaluated as

$$S_{ext}^k = \frac{cU_{ext}^k}{2} + 2 \int_{\nu_k}^{\nu_{k+1}} \int_{\pi/2}^\pi \cos \theta I_{inc}(r_{ext}, \theta, \nu, t) 2\pi \sin \theta d\theta d\nu. \quad (36)$$

For a directly driven target  $I_{inc} \simeq 0$ . For an indirectly driven capsule inside a cavity, the code approximates the incoming radiation intensity by a Planckian function corresponding to a prescribed time dependent temperature  $T_{ext}(t)$ . Because  $U^k$  is defined at cell centers,  $U_{ext}^k$  should be extrapolated from  $U_{N-1}^k$  and  $U_N^k$ . Eq. (36) becomes

$$S_{N+1}^k = \frac{c}{2} \left( U_N^k + \frac{r_{N+1} - r_N}{r_{N+1} - r_{N-1}} (U_N^k - U_{N-1}^k) - U^{P,k}(T_{ext}) \right). \quad (37)$$

For planar geometry, a similar expression is derived for  $S_1^k$ . In cylindrical and spherical geometries,  $S_1^k = 0$ . To perform a time step integration of Eqs. (27)–(29) and (37), opacity and emissivity are computed from initial values of temperature and density, but to achieve appropriate numerical stability the final temperature should be used to evaluate  $U^{P,k}$ . This quantity is linearized as

$$U^{P,k}(T_j^{e,n+1}) \simeq U^{P,k}(T_j^{e,n}) + \left( \frac{\partial U^{P,k}}{\partial T} \right)_j \left( \frac{\partial T_j^e}{\partial e_j^e} \right)_\rho (e_j^{e,n+1} - e_j^{e,n}), \quad (38)$$

where the partial derivatives are computed using the initial temperature. The system of equations then reduces to a tridiagonal linear system.

## 6. Deposition of laser energy

Laser deposition is treated in the quasi-static approximation. Energy deposition in each cell  $Q_j^{laser}$  is computed by the laser deposition subroutine on the basis of the laser pulse parameters, taking into account density and temperature profiles and ignoring retardation effects. Different laser deposition subroutines are available in the code. For situations in which the laser wavelength is of the order of the plasma scale length, the full resolution of Maxwell's equations is available, in planar geometry, for a given angle of incidence, and for either  $p$ - or  $s$ -polarization [8]. When this condition can be relaxed, as in the case of a typical IFE target, a simplified WKB approximation can be applied. In this section we derive the WKB algorithm applicable to laser beams of finite width impinging on a spherical target. Snell's law in stratified media can be written as

$$n \sin \alpha = \text{Const.}, \quad (39)$$

where  $n$  is the refractive index (vacuum light velocity  $c$  divided by light phase velocity) and  $\alpha$  is the angle between the direction of

propagation and the gradient of  $n$ . Let us introduce a mechanical analogy. The above expression is identical to the transverse momentum conservation of a fictitious “particle” of unit mass, moving in the direction of light propagation with “velocity”  $n$ , and submitted to a force in the direction of density gradient. Because, the modulus of the “velocity” depends only on  $n$ , one can state that the “force” acting on the particle derives from the “potential energy”  $-n^2/2$ . The “equation of motion” of such “particle” then takes the form

$$\frac{d^2 \vec{r}}{d\xi^2} = \frac{1}{2} \nabla n^2, \quad (40)$$

where  $\xi$  is a fictitious “time”. One can thus determine the ray trajectory by integrating this equation from the plasma boundary, where  $|d\vec{r}/d\xi| = 1$ . For an ideal plasma, the dispersion relation for electromagnetic waves with angular frequency  $\omega$  and wave number  $k$  is  $c^2 k^2 = \omega^2 - \omega_p^2$ , where  $\omega_p = \sqrt{4\pi e^2 n^e / m_e}$  is the plasma frequency and  $e$  is the electron charge. The index of refraction is  $n = ck/\omega = \sqrt{1 - \omega_p^2/\omega^2}$ . In this case, one finds that the “velocity” of the fictitious “particle” is proportional to the group velocity of the electromagnetic wave  $nc = \partial\omega/\partial k$ . On the other hand, the attenuation of power along a ray is given by [8]

$$\frac{dl}{dl} = -\frac{v^e \omega_p^2}{c \omega^2} \frac{I}{\sqrt{1 - \frac{\omega_p^2}{\omega^2}}} = -\frac{v^e}{c} \frac{1 - n^2}{n} I, \quad (41)$$

where  $v^e$  is the electron collision frequency and  $l$  is the arc length along the trajectory. This mechanical analogy leads us to find a conservation law (conservation of “angular momentum”) in spherically symmetric configurations, where  $n = n(r)$  and

$$\frac{d}{d\xi} \left( \vec{r} \times \frac{d\vec{r}}{d\xi} \right) = \frac{d\vec{r}}{d\xi} \times \frac{d\vec{r}}{d\xi} + \vec{r} \times \nabla \frac{n^2}{2} = 0, \quad (42)$$

so that  $\vec{p} = \vec{r} \times d\vec{r}/d\xi$  is constant along the ray. This implies that each ray trajectory lies in a plane containing the center of symmetry. Using polar coordinates  $(r, \theta)$  to describe the ray trajectory in this plane (see Fig. 2), one has

$$p = r^2 \frac{d\theta}{d\xi} = \text{Const.}, \quad (43)$$

$$n^2 = \left( \frac{dl}{d\xi} \right)^2 = \left( \frac{dr}{d\xi} \right)^2 + r^2 \left( \frac{d\theta}{d\xi} \right)^2. \quad (44)$$

The modulus of  $\vec{p}$  is the impact parameter of the ray; the distance of the vacuum trajectory to the target center. From these relations, the differential equations for the ray trajectory and the carried power are derived as

$$\frac{dr}{d\theta} = \frac{r}{p} \sqrt{n^2 r^2 - p^2}, \quad (45)$$

$$\frac{d \ln I}{dr} = \frac{1}{I} \frac{dl}{dr} \frac{d\xi}{d\xi} = -\frac{v^e}{c} (1 - n^2) \frac{r}{\sqrt{n^2 r^2 - p^2}}. \quad (46)$$

For a ray coming in from  $r = \infty$ , the sign of the root is negative up to the turning point, defined by the condition  $nr = p$ ; afterwards the positive sign must be taken. From Eq. (45) one concludes that the ray trajectory is symmetric with respect to the radial direction along the turning point. When Eq. (46) for the incoming ( $I^-$ ) and outgoing ( $I^+$ ) rays are added, we find

$$I^- I^+ = I_*^2, \quad (47)$$

where  $I_*$  is the power of the ray at the turning point. The above equations can be discretized by assuming that, between interfaces

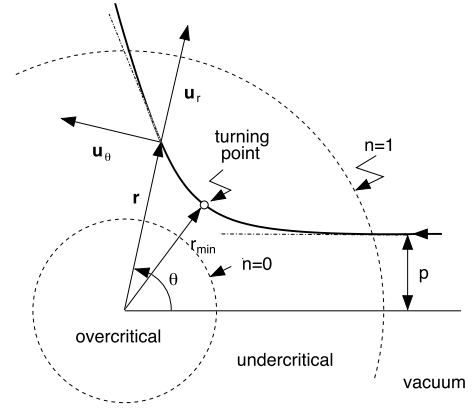


Fig. 2. Ray tracing scheme.

$j$  and  $j + 1$ , the squared refractive index (and the electron number density) varies linearly with  $r^2$ , while the electron collision frequency  $v^e$  remains constant. Setting  $n^2 = a_j r^2 + b_j$  in the equation for  $I^-$ , one has

$$\begin{aligned} \ln I_{j+1}^- - \ln I_j^- &= \frac{v_j^e}{2c} \int_{r_j}^{r_{j+1}} \frac{1 - b_j - a_j r^2}{\sqrt{a_j r^4 + b_j r^2 - p^2}} d(r^2) \\ &= \frac{v_j^e}{2c} (\Theta(a_j, b_j, -p^2, r_{j+1}^2) - \Theta(a_j, b_j, -p^2, r_j^2)), \end{aligned} \quad (48)$$

where the integral has been solved analytically in Appendix A. To evaluate  $a_j$  and  $b_j$ , the refractive index is first evaluated at cell centers and then interpolated at interfaces

$$n_j^2 = \frac{1}{2} ((n_{j-1}^{\text{cell}})^2 + (n_j^{\text{cell}})^2). \quad (49)$$

For the last interface  $n_{N+1} = 1$  is taken. The incoming beam is subdivided into a finite number of rays, each of them characterized by its impact parameter  $p$  (assumed strictly positive) and its incident power  $I_{\text{inc}}$ . Only rays with  $p < r_{N+1}$  interact with the target. Starting from the external boundary, where  $I_{N+1}^- = I_{\text{inc}}$ , Eq. (48) is applied to obtain the power at the previous interface, as long as  $n_j r_j > p$ . Because  $p > 0$ , an interface  $j_*$  where  $n_{j_*} r_{j_*} \leq p$  should always be reached. That means that the turning point is located between  $r_{j_*}$  and  $r_{j_*+1}$ , and the power there is given by

$$\ln I_{j_*+1}^- - \ln I_*^* = \frac{v_{j_*}^e}{2c} \Theta(a_j, b_j, -p^2, r_{j_*+1}^2). \quad (50)$$

The outgoing intensities are determined by Eq. (47), so that the total power across interface  $j$  is

$$I_j' \equiv I_j^+ - I_j^- = \begin{cases} 0 & \text{for } j \leq j_* \\ I_*^2 / I_j^- - I_j^- & \text{for } j > j_*. \end{cases} \quad (51)$$

Finally, the power dumped into cell  $j$  is obtained by adding contributions from all rays

$$Q_j^{\text{laser}} = \sum_{\text{rays}} (I_j' - I_{j+1}'). \quad (52)$$

Eq. (45) can be also integrated analytically to obtain the trajectory  $r(\theta)$ . Because trajectories are not needed to compute laser power deposition, details have been shifted to Appendix B.

## 7. Thermonuclear burning

A simple model of thermonuclear burning [23–25] is included in the code. Only the reaction



is taken into account, and an equimolar mixture of deuterium and tritium is assumed. The number density of both components ( $n_T = n_D$ ) is governed by the rate equation

$$\frac{\partial n_D}{\partial t} = -n_D \nabla \cdot \vec{v} - \langle \sigma v \rangle n_D^2, \quad (54)$$

where  $\vec{v}$  is the fluid velocity,  $\langle \sigma v \rangle n_D^2$  is the number of reactions per unit of time and volume, and  $\partial/\partial t$  denotes derivation with respect to individual fluid elements; i.e. at constant value of mass coordinate  $\mu$ . The reactivity is approximated by [26]

$$\langle \sigma v \rangle = C_1 \zeta^{-5/6} \xi^2 \exp(-3 \zeta^{1/3} \xi), \quad (55)$$

with

$$\zeta = 1 - \frac{C_2 T + C_4 T^2 + C_6 T^3}{1 + C_3 T + C_5 T^2 + C_7 T^3}, \quad \xi = C_0 / T^{1/3}, \quad (56)$$

where the coefficients are

$$\begin{aligned} C_0 &= 6.6610 \text{ keV}^{1/3}, & C_1 &= 643.41 \times 10^{-16} \text{ cm}^3 \text{ s}, \\ C_2 &= 15.136 \times 10^{-3} \text{ keV}^{-1}, & C_3 &= 75.189 \times 10^{-3} \text{ keV}^{-1}, \\ C_4 &= 4.6064 \times 10^{-3} \text{ keV}^{-2}, & C_5 &= 13.500 \times 10^{-3} \text{ keV}^{-2}, \\ C_6 &= -0.10675 \times 10^{-3} \text{ keV}^{-3}, & C_7 &= 0.01366 \times 10^{-3} \text{ keV}^{-3}. \end{aligned}$$

In each reaction event, a neutron and an  $\alpha$ -particle are produced. The neutron, carrying 80% of the reaction energy, is assumed to escape from the plasma without further interaction. The  $\alpha$ -particles, with initial energy and velocity,  $\epsilon_0 = 3.5 \text{ MeV}$  and  $v_0 = 1.297 \times 10^9 \text{ cm s}^{-1}$ , are treated as a supra-thermal species with energy per unit of volume  $E^\alpha$  (related to the specific energy by  $E^\alpha = \rho e^\alpha$ ). Eq. (73) of Ref. [25] is, in our notation,

$$\rho \frac{\partial}{\partial t} \left( \frac{E^\alpha}{\rho} \right) + \rho P^\alpha \frac{\partial \rho^{-1}}{\partial t} = -\nabla \cdot \vec{S}^\alpha - \frac{E^\alpha}{\tau^\alpha} + Q^\alpha. \quad (57)$$

The transfer of energy from  $\alpha$ -particles to matter is taken into account by a diffusive approach. The kinetic pressure of  $\alpha$ -particles is taken as  $P^\alpha = \frac{2}{3} E^\alpha$ ; i.e. a quasi-isotropic distribution function is assumed. The source term  $Q^\alpha = \epsilon_0 \langle \sigma v \rangle n_D^2$  is the thermonuclear power density going into  $\alpha$ -particles. The sink term  $E^\alpha / \tau^\alpha$  is the power density transferred to the plasma, that is distributed to electrons and ions, with fractions  $\phi = 33 \text{ keV} / (33 \text{ keV} + T^e)$  and  $1 - \phi$ , respectively.  $\tau^\alpha = \phi \tau^{\alpha e}$  is the relaxation time of  $\alpha$ -particles in a plasma, expressed in terms of the  $\alpha$ -particle to electron relaxation time

$$\tau^{\alpha e} = \frac{3}{16} \sqrt{\frac{2}{\pi}} \frac{a_\alpha m_p (kT^e)^{3/2}}{\log \Lambda_{\alpha e} (z_\alpha e^2)^2 n^e \sqrt{m_e}}, \quad (58)$$

with  $a_\alpha = 4$  and  $z_\alpha = 2$ . The Coulomb logarithm for this process is taken as ( $T^e$  expressed in eV, and  $n^e$  in  $\text{cm}^{-3}$ )

$$\begin{aligned} \log \Lambda_{\alpha e} & \\ &= \max \left( 2, \min \left( 23.46 - \ln \frac{\sqrt{n^e}}{(T^e)^{3/2}}, 25.26 - \ln \frac{\sqrt{n^e}}{T^e} \right) \right). \end{aligned} \quad (59)$$

For gentle gradients of  $E^\alpha$ , the energy flux carried by  $\alpha$ -particles is

$$S^\alpha = -K^\alpha \frac{\partial E^\alpha}{\partial r}, \quad (60)$$

with the diffusion coefficient

$$K^\alpha = \frac{v_0^2 \tau^{\alpha e}}{9} \left( 1 + 2 \frac{z}{a} \left( \frac{T^e}{59.2 \text{ keV}} \right)^{3/2} \right)^{-1}. \quad (61)$$

Analogous to electron heat diffusion, this flux is limited by a maximum value (all particles moving in the same direction)

$$|S^\alpha| \leq S_{max}^\alpha \equiv \frac{v_0 E^\alpha}{3}. \quad (62)$$

This limit is set using

$$\hat{K}^\alpha = \frac{K^\alpha S_{max}^\alpha}{S_{max}^\alpha + K^\alpha |\nabla E^\alpha|} \quad (63)$$

instead of  $K^\alpha$  in Eq. (60). The leakage of mass due to escaping neutrons is neglected. This is not a serious limitation for studies of marginally igniting targets; only first burning stages are considered, when the fraction of consumed fuel is still small. Fuel depletion and  $\alpha$  accumulation are taken into account, in a simplified way, by the fraction  $f$  of available reactants. Initially  $f$  is set to 1/2 for DT mixtures, and zero for non-reactive materials. Using  $n_D = n_T = 2\rho f / 5m_p$ , Eq. (54) can be written as

$$\frac{\partial f}{\partial t} = -\frac{2\rho \langle \sigma v \rangle f^2}{5m_p}. \quad (64)$$

The second term on the left hand side of Eq. (57), the compression work done by the pressure of  $\alpha$ -particles, has already been taken into account in Eq. (6) (for  $k = \alpha$ ). Because  $P^\alpha$  is also incorporated in the momentum equation (5), numerical conservation of energy is guaranteed. Only the cell values  $E_j^\alpha$  and  $f_j$  are modified by the thermonuclear burning subprocess. Eq. (64) is integrated assuming constant reactivity during the time step

$$f_j^{n+1} = \left( \frac{1}{f_j^n} + \frac{2 \langle \sigma v \rangle_j^n \rho_j^n \Delta t}{5m_p} \right)^{-1}. \quad (65)$$

Eq. (57) is discretized implicitly as

$$\begin{aligned} E_j^{\alpha, n+1} - E_j^{\alpha, n} &= (A_j^n S_j^{\alpha, n+1} - A_{j+1}^n S_{j+1}^{\alpha, n+1}) \Delta t \\ &\quad - \frac{E_j^{\alpha, n+1} \Delta t}{\tau_j^{\alpha, n}} + \frac{2\epsilon_0 \rho_j^n}{5m_p} (f_j^{n+1} - f_j^n), \end{aligned} \quad (66)$$

where the energy flux of  $\alpha$ -particles is

$$S_j^{\alpha, n+1} = -\hat{K}_j^{\alpha, n} \frac{E_j^{\alpha, n+1} - E_{j-1}^{\alpha, n+1}}{\frac{1}{2}(r_{j+1}^n - r_{j-1}^n)}. \quad (67)$$

At the capsule center, one sets  $S_1^{\alpha, n+1} = 0$ , and at the external boundary the maximum flux  $S_{max}^\alpha$  is assumed as

$$S_{N+1}^{\alpha, n+1} = \frac{v_0}{3} \left( \frac{3}{2} E_N^{\alpha, n+1} - \frac{1}{2} E_{N-1}^{\alpha, n+1} \right). \quad (68)$$

The value of  $K^\alpha$  at interfaces, required in Eq. (63), is obtained as the average of the values at the two adjacent cells, but the maximum value is taken to evaluate  $S_{max}^\alpha$ . Eqs. (66)–(68) become a tridiagonal system of linear equations. Once it has been solved, the powers to be deposited into electron and ion species are obtained as

$$Q_j^{\alpha \rightarrow e} = \frac{\phi_j^n E_j^{\alpha, n+1} V_j^n}{\tau_j^{\alpha, n}}, \quad Q_j^{\alpha \rightarrow i} = \frac{(1 - \phi_j^n) E_j^{\alpha, n+1} V_j^n}{\tau_j^{\alpha, n}}, \quad (69)$$

where  $V_j^n$  is the cell volume.

## 8. Code structure

The concept of fractional step method was introduced conceptually in Section 2. However, to implement this scheme in a practical and efficient way, several issues have to taken into account.

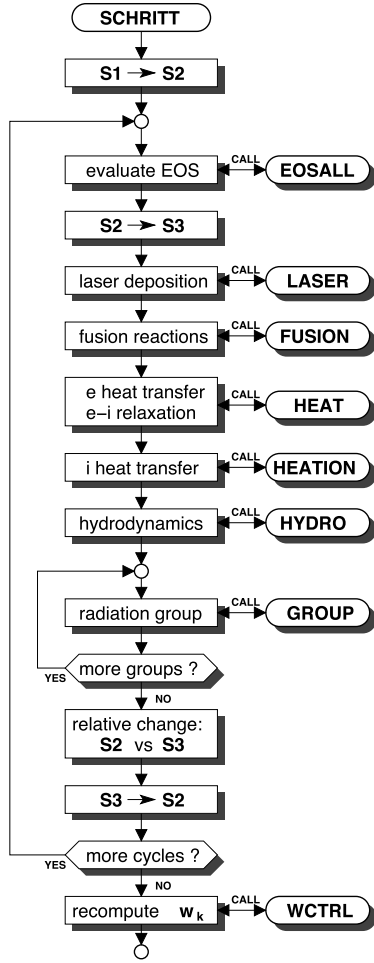


Fig. 3. Flow diagram of the integration step subroutine.

### 8.1. Subcycling

Among the physical effects considered in Sections 3–7, the most demanding one is radiation transport. For each group, Eqs. (27)–(29) must be solved to advance the specific internal energy of electrons  $e_j^e$ . For a large number of groups ( $N_G$ ), most of the computer load will be devoted to solve radiation transport. The integration interval  $\Delta t$  is usually adjusted by specifying a nominal variation of selected variables during a time step. The variations of  $e_j^e$  in each radiative subprocess are small ( $\propto N_G^{-1}$ ). The time step  $\Delta t$  is set by variations in the other subprocesses. One way to speed up the code without losing accuracy is subcycling. In the course of a time step, the advance of each non-radiative subprocess is split into  $N_S$  fractions, so that variations become also small in these subprocesses. The time step is divided into  $N_S$  subcycles. In each subcycle, all non-radiative subprocesses and a block of radiative subprocesses are advanced; groups  $k = 1, 1 + N_S, 1 + 2N_S, \dots$  in the first subcycle, groups  $k = 2, 2 + N_S, 2 + 2N_S, \dots$  in the second subcycle, and so on. If spectral properties are smooth enough, namely, if radiative properties of groups  $k$  to  $k + N_S$  are similar, these subcycles behave as effective time steps, and the change of variables during one subcycle can be used to control  $\Delta t$ .

### 8.2. Distribution of laser deposition

The simple option of dealing with laser deposition as an independent subprocess ( $e_j^{e,n+1} - e_j^{e,n} = Q_j^{laser} \Delta t$ ) has a serious

drawback. Laser deposition usually peaks in a small region where the density is close to the critical density. Direct deposition of energy would produce a large temperature peak that will be thereafter smoothed out by diffusive subprocesses. To avoid such cyclical oscillations, the laser deposition has to be coupled to the diffusive subprocesses.  $Q_j^{laser}$  is divided into  $N_G + 1$  fractions  $w_k$  that are coupled to radiation groups ( $k = 1, \dots, N_G$ ) and to electron heat transport ( $k = N_G + 1$ ). The values of  $w_k$  are adjusted dynamically in order to minimize temperature swings at the cell where specific deposition is maximum. The variation of temperature  $\Delta \tilde{T}_k$  at that cell, for subprocess  $k$ , is taken as

$$\Delta \tilde{T}_k \simeq w_k \Delta \tilde{T}_* - b_k, \quad (70)$$

where  $\Delta \tilde{T}_* = \tilde{Q}^{laser} \Delta t / \tilde{C}_v$  would be the total variation of temperature in absence of diffusion,  $\tilde{Q}^{laser}$  and  $\tilde{C}_v$  are the peak specific deposition and the isochoric specific heat capacity of the cell, and  $b_k$  accounts for temperature reduction by diffusion. Assuming slow changes of  $\Delta \tilde{T}_*$  and  $b_k$  over time, the values of  $w_k$  that will produce equal variations of temperature in all subprocesses can be estimated from variations of temperature in the previous step

$$w_k \leftarrow w_k + \frac{1}{\Delta \tilde{T}_*} \left( \frac{\sum_{k=1}^{N_G+1} \Delta \tilde{T}_k}{N_G + 1} - \Delta \tilde{T}_k \right). \quad (71)$$

Power deposition terms in Eqs. (12), (13) and (27) then become

$$\begin{aligned} Q_j^e &= w_{N_G+1} Q_j^{laser} + Q_j^{\alpha \rightarrow e}, & Q_j^i &= Q_j^{\alpha \rightarrow i}, \\ Q_j^k &= w_k Q_j^{laser}. \end{aligned} \quad (72)$$

### 8.3. Linearization of the equation-of-state

Ion and electron pressures and temperatures are obtained by interpolation in external tables as functions of the density and the specific electron and ion internal energies. That involves a time consuming fetch and evaluation procedure. To reduce the computational burden, these magnitudes are interpolated at the beginning of each subcycle and assumed to vary linearly throughout the subcycle. Likewise, ionization is interpolated and assumed to be constant throughout the subcycle.

### 8.4. Flow diagram

Fig. 3 illustrates the flow diagram of the integration step subroutine. There are two nested loops: an external one involving  $N_S$  subcycles, and an internal one involving  $N_G/N_S$  radiation groups associated with each subcycle. The names of the subroutines that implement each subprocess are indicated in the figure. **S1**, **S2**, and **S3** are the state vectors (each containing a complete set of the primary variables), at the beginning of the time step, at the beginning of a subcycle, and at the end of a subprocess, respectively. Temperature increments of the cell, where laser deposition is maximum, are monitored and used to evaluate the values of  $w_k$  to be employed in the next integration step. At the end of each subcycle, before copying **S3** into **S2**, the relative variations of selected quantities (e.g. density and temperature) are normalized with user's specified variations (typically 10%).  $\eta_{max}$ , the maximum between these values, is returned to the main program. If  $\eta_{max} \leq 2$ , the integration step is considered valid, and  $\Delta t$  is adjusted in order to get  $\eta_{max} \simeq 1$  in the next step:  $\Delta t \leftarrow \Delta t / \max(1/2, \eta_{max})$ . In addition,  $\Delta t$  is enforced to lie inside a user's defined range. On the contrary, if  $\eta_{max} > 2$ , the step is considered unsuccessful, and it is repeated with half the time step,  $\Delta t/2$ .

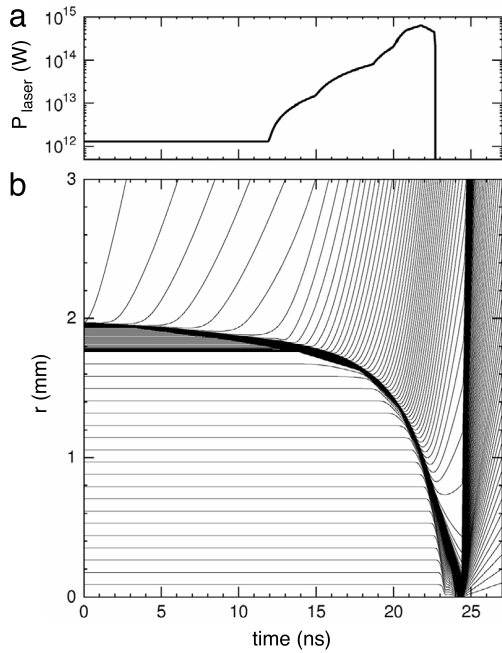


**Fig. 4.** Laser driven capsule. (a) Time dependence of the power of the laser pulse. (b) Implosion diagram.

### 8.5. Program output

In addition to deliver the main variables as functions of position and time, the code supplies the evolution of a set of magnitudes relevant for IFE studies: the average implosion velocity of the fuel, the confinement parameter  $\langle \rho R \rangle = \int_0^{r_{fuel}} \rho dr$ , the in-flight-aspect-ratio (IFAR; average shell radius divided by shell thickness), and the isentrope parameter  $\alpha$  (the average ratio of actual fuel pressure and the corresponding pressure of totally degenerated fuel at the same density). Comprehensive descriptions of all numerical options, input and output file formats, implementation, and other technical details are given in document 2015-MULTI-IFE.pdf, supplied together with the source code.

## 9. Example A: laser driven capsule

As a first example, we simulate the target configuration originally developed in [27] and described in detail in Sec. 3.1 of [3]. It consists of a hollow shell with an outer radius of 1.971 mm, composed of a 37  $\mu\text{m}$  thick layer of plastic outer ablator and a 174  $\mu\text{m}$  thick layer of cryogenic solid DT fuel. The central cavity is filled with DT vapor of 0.3  $\text{mg cm}^{-3}$ . The capsule is irradiated by a 22.7 ns long pulse of 0.25  $\mu\text{m}$  laser light with a total energy of 1.7 MJ. The pulse power changes in time as shown in Fig. 4(a). It starts with a 12 ns long prepulse of 1.3 TW, and then grows to reach a peak power of about 600 TW. The implosion is visualized in Fig. 4(b), where selected trajectories of interfaces are plotted in the radius–time plane. A large number of cells is chosen for the target shell, and the trajectories lie so dense that it appears as a black area in the figure. We see that cells at the outer surface of the capsule, heated by the laser light, vaporize, ionize, and expand. Interfaces of the heated cells are seen, peeling off from the surface and ablating outwards. Momentum conservation forces the inner, non-ablated part of the capsule to move inwards under the action of the ablation pressure. The trajectories of some of the rays belonging to one of the laser beams are shown in Fig. 5(a) at time  $t = 22.7$  ns (end of irradiation).

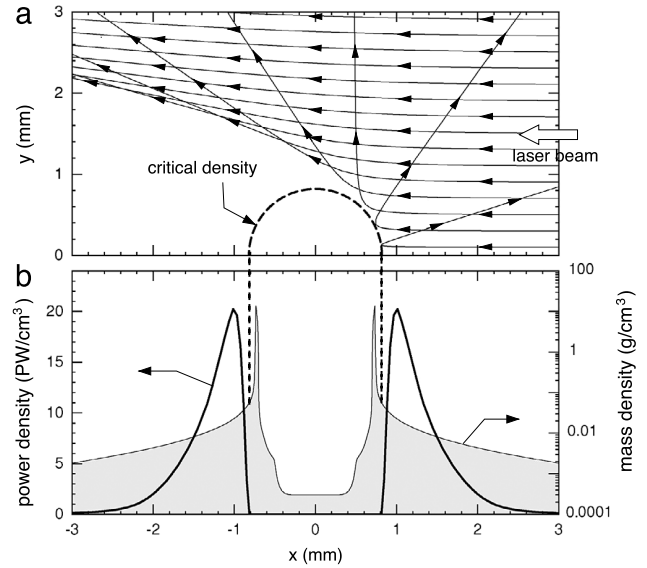


**Fig. 5.** Laser driven capsule at  $t = 22.7$  ns. (a) Some of the ray trajectories used to discretize one of the laser beams. Each trajectory has a different value of the impact parameter  $p$  (see Fig. 2). Deflection angle decreases with  $p$ , from  $180^\circ$ , for  $p = 0$ , to zero, when  $p \rightarrow \infty$ . (b) Density and laser power per unit of volume, the latter obtained by adding the contributions of a large number (100) of rays and averaging over the  $4\pi$  solid angle.

Laser cross section is taken as a super-Gaussian profile

$$I(r, t) = I_{max}(t) \exp\left(-\ln 2 \left(\frac{2r}{D}\right)^8\right), \quad (73)$$

with diameter  $D = 3.5$  mm (FWHM). Rays with normal incidence reach the critical density and are reflected back. For grazing incidence, rays deviate before reaching the critical density, and deposit their energy in low density regions. The  $4\pi$ -solid angle averaged power deposition per unit of volume is displayed in Fig. 5(b). When the pulse is switched off, the capsule has absorbed about 1.35 MJ of laser energy, and almost 90% of the plastic layer has been ablated. The shell has now imploded to half the initial radius and is coasting inwards at a velocity of  $3.8 \times 10^7$   $\text{cm s}^{-1}$ . The shocks launched during implosion, after passing the shell, run into the gas. They generate considerably more entropy in the gas than in the shell, because the density of the gas is much smaller. At stagnation time  $t = 24.30$  ns, when the imploding material piles up in the center and comes to rest, the high entropy gas reaches a temperature ( $T^e \approx T^i \approx 10$  keV) much higher than the surrounding low-entropy fuel and forms the central part of the hot spot, which serves as a spark plug for ignition. The colder fuel surrounding the hot spot has been compressed to  $\rho \approx 500$   $\text{g cm}^{-3}$ . At this moment of stagnation, when values close to maximum fuel  $\langle \rho R \rangle$  are achieved, ignition occurs in the central hot spot. A burn wave is then running outwards and ignites the whole fuel, which expands rapidly. This process is summarized in Fig. 6, showing the flow diagram (a), the evolution of the central ion temperature (b), the fuel and hot spot confinement parameters (c), and the released fusion power (d). A total of 140 MJ of fusion energy is released. When Figs. 4 and 6 are compared with Figs. 3.4 and 3.13 of Ref. [3], where results computed by code IMPL0-upgraded [25] have been plotted, it is difficult to see any difference. Nevertheless, there are some small differences: burning maximum takes place at 24.39 ns in our results instead of 24.55 ns in [3], peak  $\langle \rho R \rangle$  is 1.59  $\text{g cm}^{-2}$  instead 1.7  $\text{g cm}^{-2}$ , and peak ion temperature is 135 keV instead of 120 keV. Such discrepancies may be attributed to small differences in the two codes with respect to composition of plastic ablator,

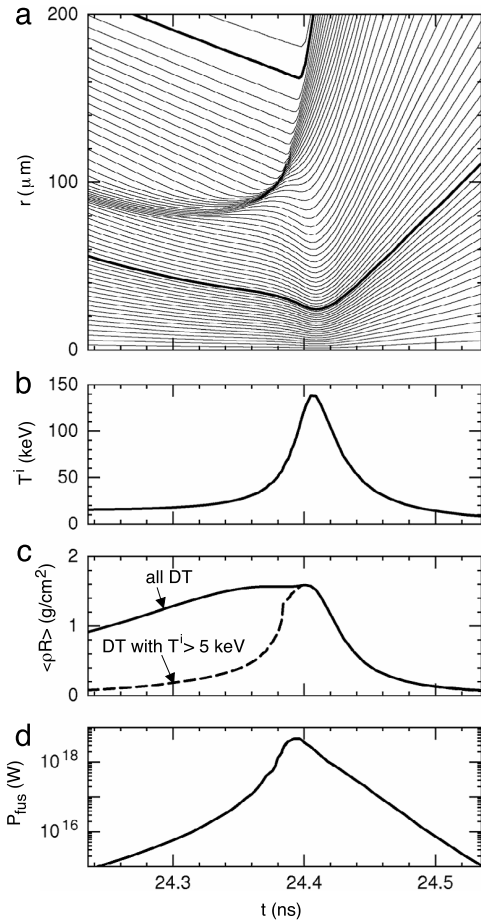


**Fig. 6.** Laser driven capsule. (a) Enlarged view of the flow chart of Fig. 4. The thick solid curves are the Lagrangian lines corresponding to the interface between initially frozen DT and vapor DT, and between DT and ablator. (b)–(d) Time evolution of relevant IFE quantities.

pulse shape, laser beam cross profile, equation-of-state, thermal flux limiter, radiation transport, reactivities, etc. Near the edge of ignition, small differences in the performance of the implosion lead to a larger difference in the thermonuclear yield: 140 MJ instead 105 MJ. However, one should take into account that thermonuclear yield is particularly sensitive to model assumptions; e.g., if flux limit factor in Eq. (17) is changed from  $f = 0.10$  to  $f = 0.03$ , yield decays from 140 MJ to 108 MJ (close to the 105 MJ reported in [3]).

**10. Example B: indirectly driven capsule**

The code MULTI-IFE has been used to simulate the implosion of the inner capsule placed in a hohlraum and driven by a pulse of thermal radiation, taken from Ref. [2]. The particular capsule design is that of Figs. 110 and 111 (pag. 4010) in [2]. Here, we assume that the capsule can be treated as hydrodynamically isolated (i.e., ignoring any interaction with the plasma of the hohlraum) and submitted to a uniform and known isotropic thermal radiation. The capsule dimensions and the temporal shape of  $T_r(t)$  are shown in Fig. 7(a) and (b). Trajectories of interfaces are plotted in Fig. 7(c) in the radius–time plane.

The dynamics of this implosion is analogous to the one in Fig. 4 of the previous section. The evolution of the internal structure of the shell, not fully resolved in 7(c), can be followed in more detail in Figs. 8 and 9, where density and ion-temperature have been plotted as functions of time and cell number.

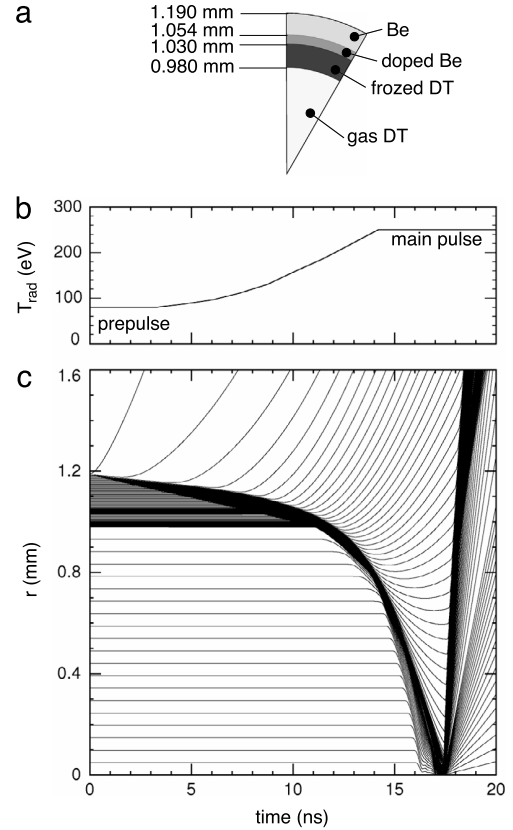


**Fig. 7.** Indirectly driven capsule. (a) Scheme of the capsule. (b) Time evolution of the temperature of the incident thermal radiation. (c) Implosion diagram.

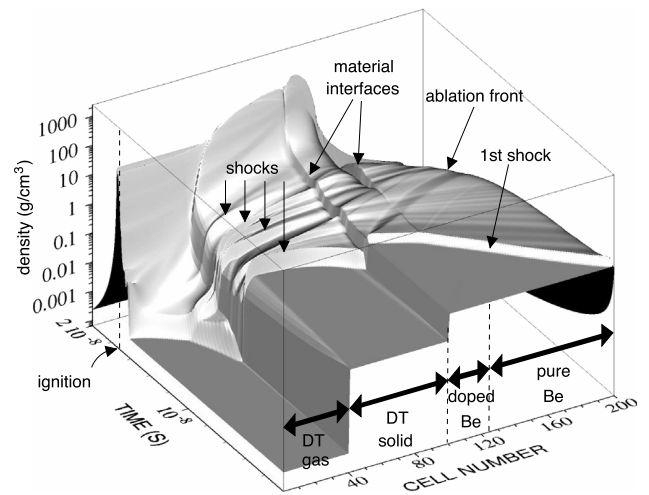


**Fig. 8.** Indirect driven capsule. Density.

Shocks and contact discontinuities between materials are seen as cliffs. The set of successive shock waves that compress the fuel in a low-adiabat mode are clearly visible. The ablation front, smoothed by multi-frequency radiation appears as a gradual transition. During the implosion phase, 182 kJ of radiation energy were absorbed, and the implosion velocity reaches up to  $2.92 \times 10^7 \text{ cm s}^{-1}$ . The imploding shell stagnates at 17.325 ns, when the peak density of DT is about  $800 \text{ g cm}^{-3}$ , the hot spot radius is  $32 \text{ }\mu\text{m}$  and the confinement parameter  $\langle \rho R \rangle$  is  $0.97 \text{ g cm}^{-2}$ . The ignition process is illustrated in Fig. 10, where successive profiles of density

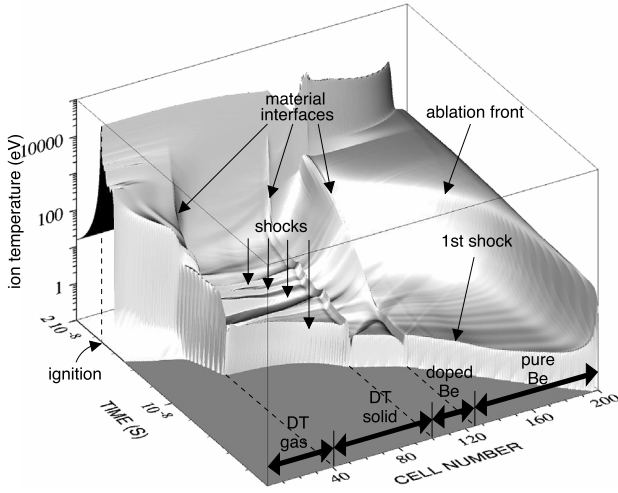


Fig. 9. Indirect driven capsule. Ion temperature.

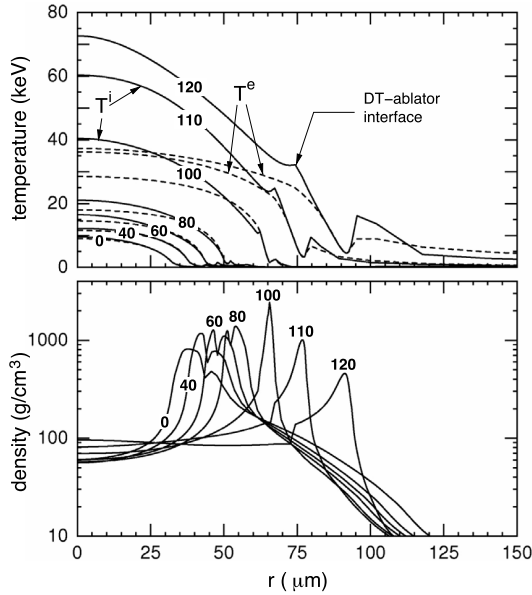


Fig. 10. Indirectly driven capsule. Temperature and density profiles during the thermonuclear burning propagation. Time labels (in ps) are relative to stagnation time  $t = 17.325$  ns.

and temperature have been plotted as functions of radius. The convergence ratio (initial radius divided by hot spot radius) is 30, and the thermonuclear yields is 13.4 MJ. The  $24 \mu\text{m}$  thick internal part of the beryllium ablator has been doped with 2.10% of bromine and 4.86% of sodium (in % of atoms). The higher opacity of this mixture suppresses preheating of the fuel and the residual ablator layer. Using only pure beryllium in the ablator, although implosion velocity would be higher ( $3.00 \times 10^7 \text{ cm s}^{-1}$ ), ignition would not occur, and only 130 kJ of fusion energy would be produced.

## 11. Conclusions

Among the open-access MULTI codes [28], the MULTI-IFE code presented here contains, well documented, the essential physics to model ignition and thermonuclear burn of inertial confinement fusion, be it in one-dimensional geometry and thus leaving aside important multi-dimensional effects such as hydrodynamic instabilities and mixing. At a time, when the central question of

how much driver energy is actually required for stable ignition and gain is still a matter of world-wide research, the present code may help to explore new target designs and to make such studies accessible to a broad international community. For example, laser direct drive may be reconsidered as a promising option, possibly making use of shock ignition [29,30], and the MULTI-IFE option for ray tracing should be helpful in this respect. Multi-group radiation transport is another strong feature of this code. In addition, all the physical processes available in [8] have been included, so that MULTI-IFE can be used in a wide range of applications, for example, laser-matter interaction at moderate intensity. The code allows to obtain quick answers: the simulations presented in Sections 9 and 10 require CPU times of 13 and 18 s on an ordinary laptop, respectively. Another major advantage of the code lies in its versatility that makes it easy to modify and adjust it to user's needs.

## Acknowledgments

This research has been supported by CICYT of Spain projects ENE 2006-06339 and ENE 2009-11668, and by the EURATOM associations CIEMAT and Max-Planck-Institut für Plasmaphysik in the framework of the 'IFE Keep-in-Touch Activities'. The authors would like to express their thanks to Mauro Temporal, Fuyuan Wu, and Zheyi Ge for many useful discussions during the development of this work.

## Appendix A

The integral in Eq. (48) can be expressed as

$$\Theta(a, b, c, x) \equiv \int_{x_{\min}}^x \frac{1 - b - ax}{\sqrt{ax^2 + bx + c}} dx, \quad (74)$$

where  $x_{\min}$  is the smaller positive value with  $ax^2 + bx + c \geq 0$ . This turning point exists because  $ax^2 + bx + c \equiv n^2x - p^2$  is negative at  $x = 0$  and positive for some value of  $x$  (light propagation should occur somewhere). To evaluate the integral one sets

$$\Theta(a, b, c, x) = (1 - b/2) \Theta'(a, b, c, x) - \sqrt{ax^2 + bx + c},$$

$$\Theta'(a, b, c, x) \equiv \int_{x_{\min}}^x \frac{dx}{\sqrt{ax^2 + bx + c}}. \quad (75)$$

For  $a = 0$ , one has

$$\Theta'(0, b, c, x) = \frac{2}{b} \sqrt{bx + c}. \quad (76)$$

For  $a \neq 0$ , the transformation  $u = (2ax + b)/\sqrt{b^2 - 4ac}$ , that maps  $x_{\min}$  into  $u = 1$ , leads to

$$\Theta'(a, u) = \begin{cases} \frac{1}{\sqrt{a}} \int_1^u \frac{du}{\sqrt{u^2 - 1}} = \frac{1}{\sqrt{a}} \log(\sqrt{u^2 - 1} + u) & (a > 0) \\ \frac{1}{\sqrt{-a}} \int_u^1 \frac{du}{\sqrt{1 - u^2}} = \frac{1}{\sqrt{-a}} \arccos u & (a < 0). \end{cases} \quad (77)$$

## Appendix B

Eq. (45) can be integrated to give the polar angle in function of radius

$$\theta = \int \frac{p}{\sqrt{r^2 n^2 - p^2}} \frac{dr}{r} = \frac{p}{2} \int \frac{1}{\sqrt{ax^2 + bx + c}} \frac{dx}{x}$$

$$= \mp \frac{p}{2} \frac{1}{\sqrt{-c}} \arccos \left( \frac{bx + 2c}{x\sqrt{b^2 - 4ac}} \right) + \text{Const.}$$

$$= \mp \frac{1}{2} \arccos \left( \frac{2p^2/r^2 - b}{\sqrt{b^2 + 4ap^2}} \right) \equiv \mp \Phi(a, b, p, r). \quad (78)$$

The constant was chosen so that  $\theta = 0$  corresponds to the minimum value of  $r$ . The sign is negative/positive for incoming/outgoing rays. To obtain the trajectory, one starts from entry point where,  $\theta_{N+1} = \arcsin(p/r_{N+1})$ . For each cell with  $n_j r_j > p$ , one has

$$\theta_j = \theta_{j+1} + \Phi(a_j, b_j, p, r_{j+1}) - \Phi(a_j, b_j, p, r_j). \quad (79)$$

If  $n_j r_j \leq p$ , the turning point is located between  $r_j$  and  $r_{j+1}$ , and its polar coordinates are

$$\theta^* = \theta_{j+1} + \Phi(a_j, b_j, p, r_{j+1}), \quad (80)$$

$$r^* = \sqrt{\sqrt{\frac{b_j^2}{4a_j^2} + \frac{p^2}{a_j}} - \frac{b_j}{2a_j}}. \quad (81)$$

The outgoing trajectory  $r'(\theta)$  is symmetric, respect to the line defined by  $\theta^*$

$$r'_j = r_j, \quad \theta'_j = 2\theta^* - \theta_j. \quad (82)$$

## References

- [1] J.H. Nuckolls, L. Wood, A. Thiessen, G.B. Zimmermann, *Nature* 239 (1972) 129.
- [2] J. Lindl, *Phys. Plasmas* 2 (1995) 3933.
- [3] S. Atzeni, J. Meyer-ter-Vehn, *The Physics of Inertial Fusion*, Oxford Science Publications, Oxford, 2004.
- [4] J.D. Lindl, P. Amendt, R.L. Berger, S.G. Glendinning, S.H. Glenzer, S.W. Haan, R.L. Kauffman, O.L. Landen, L.J. Suter, *Phys. Plasmas* 11 (2004) 339–491.
- [5] J. Lindl, O. Landen, J. Edwards, E. Moses, NIC team, *Phys. Plasmas* 21 (2014) 020501.
- [6] R. Ramis, R.J. Schmalz, J. Meyer-ter-Vehn, *Comput. Phys. Comm.* 49 (1988) 475–505.
- [7] K. Eidmann, J. Meyer-ter-Vehn, T. Schlegel, S. Hüller, *Phys. Rev. E* 62 (2000) 1202–1214.
- [8] R. Ramis, K. Eidmann, J. Meyer-ter-Vehn, S. Hüller, *Comput. Phys. Comm.* 183 (2012) 637–655.
- [9] M. Tabak, D. Callahan-Miller, *Phys. Plasmas* 5 (1998) 1895.
- [10] R.A. Vesey, M.C. Herrmann, R.W. Lemke, M.P. Desjarlais, M.E. Cuneo, W.A. Stygar, G.R. Bennett, R.B. Campbell, P.J. Christenson, T.A. Mehlhorn, J.L. Porter, S.A. Slutz, *Phys. Plasmas* 14 (2007) 056302.
- [11] R. More, K.H. Warren, D.A. Young, G. Zimmermann, *Phys. Fluids* 31 (1988) 3059–3078.
- [12] A. Kemp, J. Meyer-ter-Vehn, *Nucl. Instrum. Methods A* 415 (1998) 674.
- [13] R.D. Richtmyer, K.W. Morton, *Difference Methods for Initial Value Problems*, Interscience, New York, 1976.
- [14] S.I. Braginskii, in: M.A. Leontovich (Ed.), *Reviews of Plasma Physics*, vol. 1, Consultants Bureau, New York, 1995, pp. 205–311.
- [15] R.C. Malone, R.L. McCrory, R.L. Morse, *Phys. Rev. Lett.* 34 (1975) 721–724.
- [16] A. Sunahara, J.A. Delettrez, C. Stoeckl, R.W. Short, S. Skupsky, *Phys. Rev. Lett.* 91 (2003) 095003.
- [17] J.J. Duderstadt, G.A. Moses, *Inertial Confinement Fusion*, Wiley & Sons, New York, 1982.
- [18] A. Tronnier, *Absorption von VUV-Photonen in warm dense matter* (Ph.D. thesis), Technical University Munich, 2006.
- [19] J. Meyer-ter-Vehn, A. Tronnier, Y. Cang, *Europhysics Conference Abstracts*, 35th EPS Conference on Plasma Physics. Hersonissos, vol. 32, 9–13 June, 2008, P-2.132.
- [20] G.D. Tsakiris, K. Eidmann, *J. Quant. Spectrosc. Radiat. Transfer* 38 (1987) 353–368.
- [21] K. Eidmann, *Laser Part. Beams* 12 (1994) 223–244.
- [22] Y.B. Zel'dovich, Y.P. Raizer, *Physics of Shock Waves and High-Temperature Phenomena*, Academic Press, New York, 1966.
- [23] S. Atzeni, A. Caruso, *Il Nuovo Cimento* 64 (1981) 383–395.
- [24] S. Atzeni, *Comput. Phys. Comm.* 43 (1986) 107–125.
- [25] S. Atzeni, *Plasma Phys. Control. Fusion* 29 (1987) 1535–1604.
- [26] H.-S. Bosch, G.M. Hale, *Nucl. Fusion* 32 (1992) 611–631.
- [27] R.L. McCrory, C.P. Verdon, in: A. Caruso, E. Sindoni (Eds.), *Inertial Confinement Fusion*, in: *Proceedings of the Course and Workshop*, Società Italiana di Fisica, Bologna, Villa Monastero, Varenna, Italy, 1989, pp. 83–123. 6–16 September. <http://server.faiia.upm.es/multi/>, 2015.
- [28] R. Betti, C.D. Zhou, K.S. Anderson, L.J. Perkins, W. Theobald, A.A. Solodov, *Phys. Rev. Lett.* 98 (2007) 155001.
- [30] S. Atzeni, X. Ribeyre, G. Schurtz, A. Schmitt, B. Canaud, R. Betti, L. Perkins, *Nucl. Fusion* 54 (2014) 054008.